INTERNATIONAL JOURNAL OF
Minerals, Metallurgy and Materials

Volume 31, Number 1, January 2024
Page 118

Research Article https://doi.org/10.1007/s12613-023-2747-x

Microstructure and thermal properties of dissimilar M300–CuCr1Zr alloys by multi-material laser-based powder bed fusion

Xiaoshuang Li[1)], *Dmitry Sukhomlinov*[2)], *and Zaiqing Que*[3),✉]

1) Aerosint SA, B-4040 Herstal, Belgium
2) Aalto University, Department of Chemical and Metallurgical Engineering, Espoo 02150, Finland
3) VTT Technical Research Centre of Finland, Espoo 02044, Finland

(Received: 26 June 2023; revised: 21 August 2023; accepted: 15 September 2023)

Abstract: Multi-material laser-based powder bed fusion (PBF-LB) allows manufacturing of parts with 3-dimensional gradient and additional functionality in a single step. This research focuses on the combination of thermally-conductive CuCr1Zr with hard M300 tool steel. Two interface configurations of M300 on CuCr1Zr and CuCr1Zr on M300 were investigated. Ultra-fine grains form at the interface due to the low mutual solubility of Cu and steel. The material mixing zone size is dependent on the configurations and tunable in the range of 0.1–0.3 mm by introducing a separate set of parameters for the interface layers. Microcracks and pores mainly occur in the transition zone. Regardless of these defects, the thermal diffusivity of bimetallic parts with 50vol% of CuCr1Zr significantly increases by 70%–150% compared to pure M300. The thermal diffusivity of CuCr1Zr and the hardness of M300 steel can be enhanced simultaneously by applying the aging heat treatment.

Keywords: multi-material additive manufacturing; laser-based powder bed fusion; thermal diffusivity; dissimilar metals; copper alloy

1. Introduction

Additive manufacturing (AM) refers to digital manufacturing processes where an object is manufactured in a layer-by-layer approach, which significantly shortens development cycles and lead time. As the most matured metal AM technology, laser-based powder bed fusion (PBF-LB) has the unique advantage of making parts with unprecedentedly complex geometries. It allows mould makers to design and produce high performance moulds with integrated conformal cooling channels [1–2] and minimal drilling of hard materials.

High carbon steels (H13 [3] and M2 [4]) and maraging steels (M300 [5]) are the tool steels commonly used in the mould making industry due to their high hardness and wear resistance. In the PBF-LB process, rapid solidification and cooling lead to large thermal gradient and high residual stress, therefore preheating up to a few hundred degrees is required to manufacture crack-free high carbon steels [6]. In contrast, the maraging steel (M300) has good processibility without preheating, and it has been already used in many applications such as hot-work dies [5], tools, and moulds [6].

To add more functionality to additively manufactured components and to achieve superior properties that are impossible for single materials, researchers have made tremendous efforts to make multi-material parts by PBF-LB [7–14]. A typical example is to combine structural materials with thermally conductive Cu-based materials, such as W–CuSn10 [15], 316L–bronze [16–19], 316L–CuCr1Zr [20–21], M300–CuCr1Zr [12,22], and 420SS–Cu [23]. Although pure Cu is an attractive material for thermal applications, printing fully dense Cu parts is very challenging due to its low absorption of infrared (IR) light and a narrow processing window [24–25]. In comparison with processable bronze, Cu alloys including CuCr1Zr [26–28] and CuNi2SiCr [29] have much higher thermal conductivity and reasonably good processibility with high-power IR laser. Consequently, it is of great interest to combine M300 steel with CuCr1Zr. However, very limited amount of research on combining CuCr1Zr alloy and maraging steels via PBF-LB has been conducted [12,22]. Moreover, these works were performed in a less efficient mode since powders were sequentially deposited at each layer. The fully automated selective powder deposition (SPD) system developed by Aerosint [30] enables simultaneous deposition of multiple powders with any patterns, which fulfills the demand for a compositional gradient in all three dimensions. In addition, thermal diffusivity can be doubled by replacing 50vol% of maraging steel with CuCr1Zr [31]. However, some large defects were observed in the preliminary work, which deteriorates thermal conduction across the interface. The essential correlation among interface processing parameters, microstructure, and thermal properties remains unrevealed.

This work aims to initiate the development of multi-ma-

✉ Corresponding author: Zaiqing Que E-mail: zaiqing.que@vtt.fi

Springer

terial industrial applications using the state-of-the-art technology, an automated single-step PBF-LB process. It focuses on the investigation of the microstructure, hardness mismatch, and thermal properties at the interface between M300 and CuCr1Zr. Special processing parameters were preliminarily introduced at the interface, and their influence on the microstructure, mechanical, and thermal properties was studied. Different interface configurations (M300 on CuCr1Zr and CuCr1Zr on M300) were designed and analyzed to gain complementary understanding of the process.

2. Experimental

2.1. Material and manufacturing process

All the M300–CuCr1Zr samples were produced with an Aconity MIDI+ (Aconity3D GmbH, Germany) equipped with an Aerosint SPD v1 recoater (Aerosint SA, Belgium), enabling manufacturing of multi-material parts by PBF-LB. The M300 powder of 15–45 μm was supplied by Carpenter Additive, UK, and the CuCr1Zr powder of –32 μm was from Eckart TLS GmbH, Germany. The chemical compositions are listed in Table 1.

The SPD recoater (Fig. 1(a)) consists of two rotatable drums covered with meshes where powders are mechanically attached under pressure. Powders are stored in the reservoirs and can flow onto the meshes by gravity. As the drums move to above a build plate, powders can be simultaneously and selectively ejected by opening valves assembled at the bottom of the drums. The rotation of drums allows powders to cover the meshes and guarantees sufficient powder supply. The selective opening of valves is determined by two CAD designs, one for each material/drum. As a result, it gives two patterns with many pixels of approximately 0.5 mm × 0.5 mm. A thin powder layer on the build plate has a tunable thickness in the range of 175–250 μm. The excessive powder is subsequently removed by a so-called leveler system to reach the desired layer thickness of 40 μm. A multi-material powder bed is formed layer by layer.

Table 1. Chemical compositions of the M300 and CuCr1Zr powders wt%

Samples	Fe	Cr	Ni	Mo	Mn	Si	N	Cu	C	Ti	Co	Zr
M300	Bal.	0.25	19.0	5.2	0.15	0.10	0.10	—	0.03	1.2	10	—
CuCr1Zr	0.02	0.91	—	—	—	≤0.004	—	Bal.	—	—	—	0.1

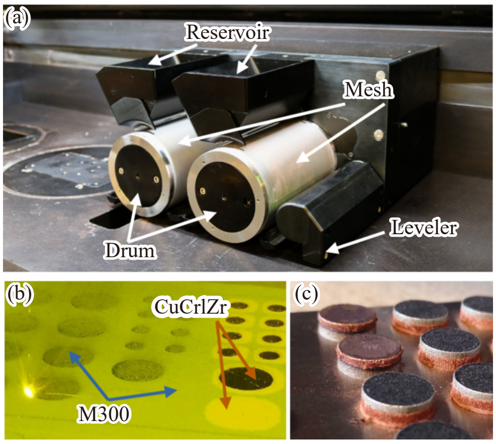

Fig. 1. (a) Two-material SPD recoater consisting of two powder reservoirs, meshes, drums, and one leveler, (b) M300–CuCr1Zr multi-material powder bed, and (c) cylindrical M300–CuCr1Zr specimens with different configurations for laser flash analysis.

The continuous Yb fiber laser has a wavelength of 1070 nm and a spot size of 80 μm. Since the CuCr1Zr alloy and M300 steel are dissimilar materials in terms of absorptivity of IR light and thermal conductivity, distinctly different processing parameters were developed in the previous work [31] (Table 2). For CuCr1Zr, a laser power of 500 W, a scanning speed of 550 mm·s^{-1} for the first melting and 600 mm·s^{-1} for the remelting with a rotation by 90° were applied, in which the remelting strategy was introduced to ensure a stable manufacturing process as well as high bulk density. Much lower energy input is needed for M300 (200 W and 700 mm·s^{-1}). The hatch distance for CuCr1Zr and M300 is 120 and 80 μm, respectively. A bi-directional simple scanning strategy and the interlayer rotation of 67° were selected in this work. To minimize oxidation, Ar inert gas was used to keep the O_2 concentration (wt%) below 800 × 10^{-6} in the entire process. All samples were manufactured on a build plate made of 316L stainless steel and machined off via electrical discharge machining (EDM).

The parameters in Table 2 were developed for making dense single-material parts. However, such parameters lead to lack-of-fusion defects locating at the interface region of M300 built on CuCr1Zr [31], suggesting that the energy input is insufficient due to the high thermal conductivity of CuCr1Zr beneath the interface. Taking the thermal conductivity of base materials into account, it is necessary to investigate the influence of different sets of parameters on the interface integrity. In the case of M300 built on CuCr1Zr, high laser power or energy input was selected, while low laser

Table 2. Summary of the process parameters

Materials	Power / W	Layer thickness / μm	Hatch distance / μm	Speed / (mm·s^{-1})	
				First melt	Remelt
M300	200	40	80	700	—
CuCr1Zr	500	40	120	550	600

power or energy input was selected when CuCr1Zr was built on M300. It is noted that the interface parameters were only applied to a few layers (3 or 10) after switching materials along the build direction (BD). However, it is not the focus to optimize the number of layers in this work where different parameters should be applied. Except the interlayer rotation of 90°, cubic specimens were manufactured with the same scanning strategy as described in the above discussion. In total, 11 different interface parameters were covered in this preliminary study and are available in Table 3.

Table 4 demonstrated the interface parameters of three samples including M300 on CuCr1Zr with interface parameters (Sample 1), CuCr1Zr on M300 with (Sample 2) and without (Sample 3) interface parameters. All these samples are cylindrical with diameter of 12.7 mm and overall height around 3.55–3.85 mm, which is the standard sample geometry for thermal diffusivity measurement detailed in the section 2.3. The volume fraction of CuCr1Zr in each M300–CuCr1Zr sample is approximately 50vol%. The configuration of M300 on CuCr1Zr without interface parameters was studied in the previous work [31].

For both materials, it is well known that post aging heat treatment is required to improve the hardness of M300 and the thermal diffusivity of CuCr1Zr. Therefore, some specimens were heat treated in a furnace at 520°C for 1 h as such parameters were proven to be effective in the previous study [31]. Besides, this allows direct comparison of the results from the present work with the ones from [31]. The furnace was preheated to 520°C before the specimens were transported into the furnace. The temperature during aging was monitored using thermocouples and stayed within about ±1°C during the thermal treatment. The aging cycle was completed with air cooling. Pickling was performed to remove the oxide layers on the specimens before the thermal diffusivity measurements and microstructural characterizations.

Table 3. Summary of defect density as a function of selected interface parameters

Configurations	Power / W	Speed / (mm·s^{-1})		Number of layers	Defect density / %
		First melt	Remelt		
M300 on CuCr1Zr	200	650	—	3	0.73
	200	600	—	3	0.36
	225	775	—	3	0.32
	225	675	—	3	0.30
	250	875	—	3	0.03
CuCr1Zr on M300	500	600	—	5	0.61
	500	600	—	10	0.35
	500	600	750	5	0.51
	500	600	750	10	0.45
	400	600	650	5	0.13
	400	600	650	10	0.04

Table 4. Summary of the sample conditions

Sample	Configurations	Interface parameters	Number of layers
1	M300 on CuCr1Zr	250 W, 875 mm·s^{-1}	3
2	CuCr1Zr on M300	400 W, 600 (Remelt: 650) mm·s^{-1}	10
3		—	—

2.2. Characterization

The as-built cubic specimens manufactured with interface parameters were sectioned and metallographically prepared for obtaining optical images at the interface regions using inverted optical microscope Olympus$^{\text{TM}}$ GX53 (Olympus Inc., Tokyo, Japan). Based on these images, defect density was quantified using ImageJ software.

The microstructure was characterized with scanning electron microscopy (SEM). The last step of the surface preparation of the cross-sectional samples was with a non-crystallizing amorphous colloidal silica suspension (0.04 μm). A Zeiss Crossbeam 540 SEM equipped with a solid-state four-quadrant backscatter detector (BSD) and an EDAX Hikari Plus electron backscatter diffraction (EBSD) detector was used. Backscatter electron (BSE) images were conducted at an accelerating voltage of 15 keV with a working distance (WD) of 5–6 mm. EBSD mapping was conducted at an accelerating voltage of 20 keV and a WD of 13–14 mm with 70° tilting, a probe current of 3 nA, and a step size of 100 nm. The obtained EBSD data was analyzed by TSL OIM Analysis 8.6 software, and the results are plotted in band-contrast image quality (IQ) map, inverse pole figure (IPF), kernel average misorientation (KAM), and phase maps.

2.3. Hardness and thermal properties

A Durascan 80 was employed to measure the microhardness of HV$_{0.1}$ and HV$_{0.01}$ across the material interface where the indentation spacing was 0.25 and 0.05 mm, respectively. The microhardness measurement was carried out on the cross-sectional samples for microstructure analysis.

The thermal diffusivity was measured in the LFA 427 Netzsch apparatus (Netzsch-Feinmahltechnik GmbH, Selb, Germany). In the experiment, a laser pulse heats a specimen from the front side and a detector on the back side measures the time dependent temperature rise. To ensure good absorption of the laser light, a thin layer of graphite was sprayed on the sample surface. Multi-layer model (two layers) by Netzsch was selected with a laser voltage of 650 V and a pulse width of 0.5 ms. The thickness of each layer was measured with a digital caliper accurately (±0.05 mm). The density used in the thermal diffusivity calculation for M300 steel and CuCr1Zr are 8.02 and 8.83 $g\cdot cm^{-3}$, respectively. The furnace chamber was evacuated and then backfilled with a 50 $mL\cdot min^{-1}$ N_2 flow during the measurement. For each material condition, 2–3 specimens were used to measure the thermal diffusivity at 50, 100, 150, 200, 250, and 300°C with a heating rate of 5 $°C\cdot min^{-1}$. The temperature of 50–300°C covers the temperature range in the targeted industrial application. The specific heat capacity (C_p) of M300 steel and CuCr1Zr are 0.399–0.516 and 0.345–0.417 $J\cdot g^{-1}\cdot K^{-1}$ at 50–300°C, respectively, while a linear thermal expansion was assumed. At each temperature, the measurement was repeated for 5 times both during the heating and cooling stages. Negligible differences between those measured on the heating and cooling cycles were observed. Results are also independent on the materials face the laser. For Sample 3, two tests were run with the CuCr1Zr facing the laser, and one test was run with the M300 facing the laser. The difference was negligible. Therefore, all the measurements were conducted CuCr1Zr facing the laser.

3. Results and discussion

3.1. Interface defect density

Table 3 tabulates the defect density of specimens manufactured using different interface parameters. For specimens with the configuration of M300 on CuCr1Zr, the defect density decreases as the power and/or line energy (power/speed) input increases. On the contrary, the CuCr1Zr on M300 specimens show that a decrease in laser power and line energy input leads to the reduction in defect density. Interestingly, there is a tendency that interface parameters need to be applied to more layers in order to achieve lower defect density. As can be seen, the optimized parameters are 250 W, 875 $mm\cdot s^{-1}$, 3 layers and 400 W, 600 (Remelt: 650) $mm\cdot s^{-1}$, 10 layers for M300 on CuCr1Zr and CuCr1Zr on M300, respectively.

3.2. Hardness measurement

The microhardness of $HV_{0.1}$ and $HV_{0.01}$ across the M300–CuCr1Zr interface in the as-built Samples 1–3 are plotted in Fig. 2(a)–(b). Both $HV_{0.1}$ and $HV_{0.01}$ show a sharp drop from an average of HV 450 for pure M300 down to HV 100 for CuCr1Zr base metal (BM). Furthermore, there is a significant difference in the width of the transition zone of the three samples. Transition zone refers to the region between two BMs where the hardness gradient is observed. The transition zone in Sample 1 is around 225 μm as observed in Fig. 2(b). In contrast, Fig. 2(a) shows a remarkably large transition zone with 1.25 mm in Sample 2 and 1.75 mm in Sample 3, respectively. It is noteworthy that the transition zone in Sample 1 and Samples 2−3 is on the M300 steel side and the CuCr1Zr side, respectively.

Fig. 2(c)–(d) depicts the microhardness of $HV_{0.1}$ and $HV_{0.01}$ across the interface in the aging treated Samples 1−3. After aging heat treatment, the average microhardness of M300 and CuCr1Zr BM increases from HV 450 to HV 600 and from HV 100 to HV 200, respectively. Similar to the case as before aging heat treatment, the transition zone is on the M300 side for the Sample 1 and on the CuCr1Zr side for the Sample 2−3. However, the hardness mismatch gradient occurs in a narrower region, suggesting that the transition zone was significantly reduced, particularly for Samples 2 from roughly 1.25 to 0.2 mm and Sample 3 from 1.75 to 0.3 mm, respectively. In Sample 1, it remains around 200−225 μm.

The hardness increase in the M300 BM results from the combination of aging hardening caused by precipitation of finely dispersed nano Ni_3Ti particles and martensitic transformation during air cooling [32–33]. This assures excellent wear [34] and fretting resistance, and fulfills the requirements in the plastic injection moulding industry. Similarly, it has been reported that the CuCr1Zr alloy can be strengthened by the grown pure Cr particles and the precipitated intermetallic compounds such as $Cu_{51}Zr_{14}$ and $Cu_{10}Cr_7$ [35–36] during aging heat treatment.

Very importantly, it is worth emphasizing that the hardness of CuCr1Zr regions in the transition zone (0.3–0.4 mm) of as-built Samples 2 and 3 reaches HV 200 without post aging heat treatment, and it stays the same after aging. Note that the CuCr1Zr BM after aging heat treatment has the same hardness of approximately HV 200. This implies that the CuCr1Zr in those regions has undergone aging hardening in the manufacturing process. It is highly likely that the low thermal conductivity of M300 beneath CuCr1Zr leads to heat accumulation at the interface, which can cause local intrinsic heat treatment (IHT) [37] by the cyclic re-heating from the subsequent layers. Thus the transition zone width is smaller in Sample 2 than Sample 3 because of the reduction in energy input at the interface.

3.3. Microstructural investigation

The microstructure across the interface of as-built Sample 3 (CuCr1Zr on M300 without parameters optimization) is shown in Fig. 3. SE and BSE image (Fig. 3(a)–(c)) shows the transition zone of 1.75 mm in the CuCr1Zr alloy and an interface mixing zone of 300 μm. The region where two materials are extensively intermixed at the interface is termed as mixing zone. The transition zone consists of mixing zone and heat affected zone (HAZ). In the context of this work, a HAZ represents the area inside the transition zone where the grain microstructure is different as compared to the rest of the

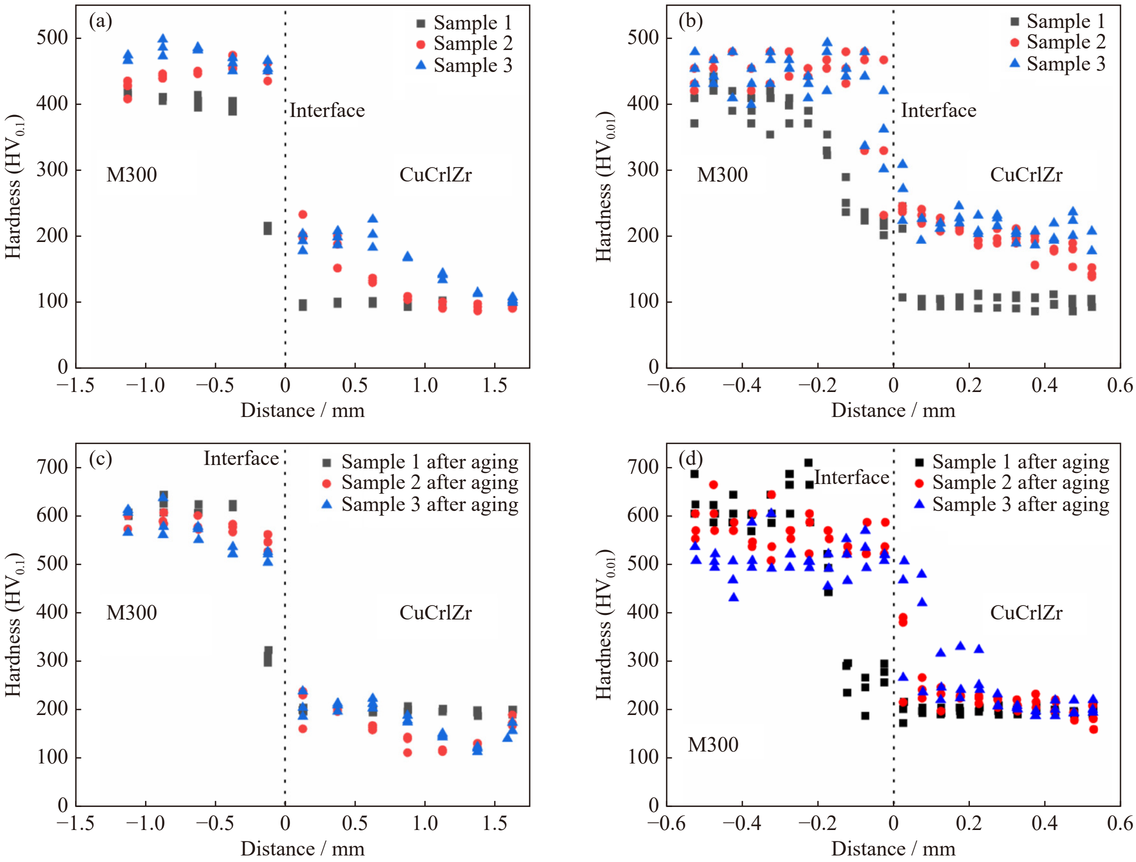

Fig. 2. $HV_{0.1}$ and $HV_{0.01}$ across the interface between the M300 and CuCr1Zr (a–b) before aging heat treatment and (c–d) post aging heat treatment, respectively.

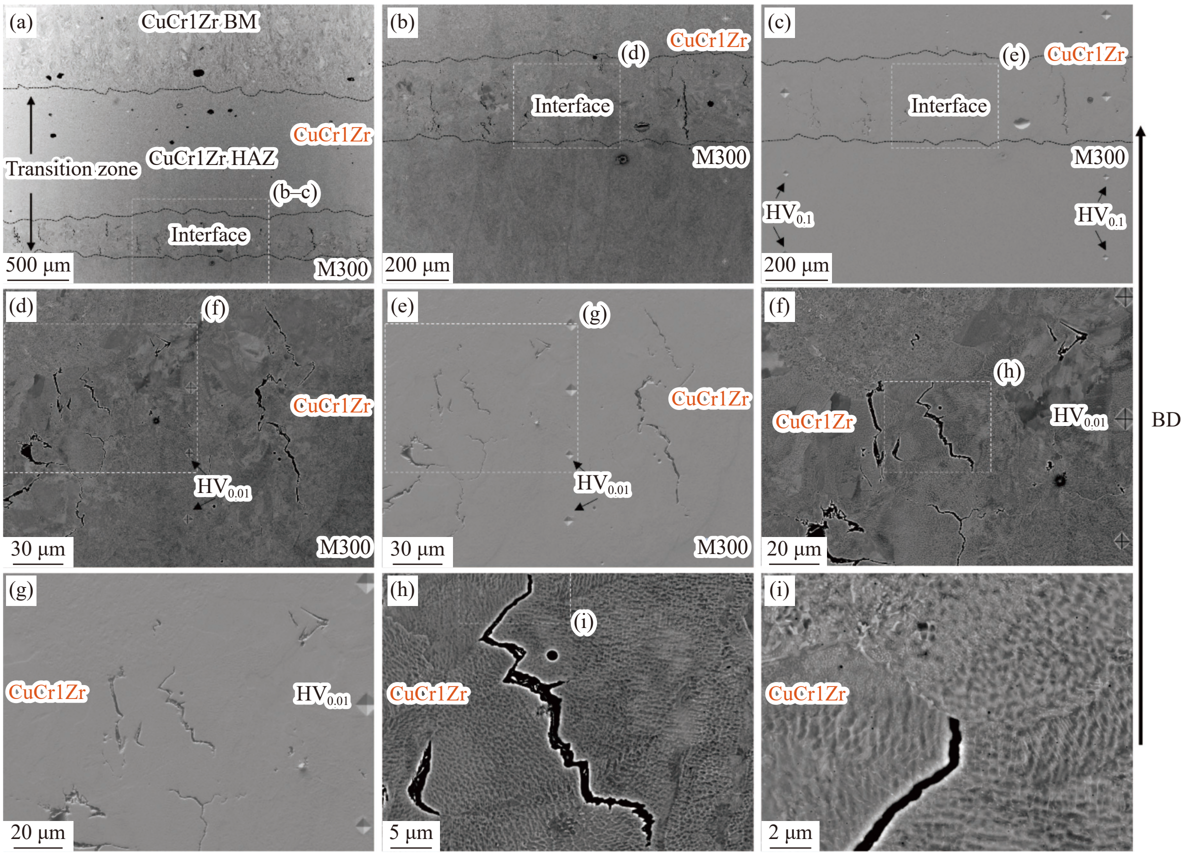

Fig. 3. (a, c, e, g) SE images and (b, d, f, h, i) BSE images of the interface between the M300 steel and CuCr1Zr of Sample 3 (CuCr1Zr on M300 and non-optimized) before aging heat treatment.

sample. The CuCr1Zr HAZ seems to have finer grains than the CuCr1Zr BM, which can explain the higher hardness in CuCr1Zr HAZ than that in the BM. It can be found that pores with a diameter up to 100 μm were observed in the HAZ and even in the BM of CuCr1Zr alloy. Some defects like microcracks with a length up to 250 μm appear only in the interface mixing zone but neither inside the HAZ nor in the CuCr1Zr BM. Fig. 3(d)–(i) displays the representative cracks in this sample located at the boundaries between dendrites with different orientations.

More in-depth characterizations were performed on as-built Samples 1–2 with parameters optimization. The microstructure across the interface of Sample 2 (CuCr1Zr on M300 with parameters optimization) before aging is shown in Fig. 4. Fig. 4(a)–(c) reveals HAZ of around 1.25 mm in the CuCr1Zr alloy and interface mixing zone of 100 μm. A few pores with a diameter up to 70 μm can be observed in the HAZ and in the interface mixing zone but no pores in the CuCr1Zr BM. There are some small cracks with a length up to 50 μm in the interface mixing zone. However, both the HAZ and the BM of CuCr1Zr alloy are free of cracks. Compared with Sample 3, Sample 2 has much lower crack density. The defect density determined as the area fraction of cracks and pores observed at the interface mixing zone is 0.28% and 0.66% for Samples 2 and 3, respectively.

The processing parameters optimization is favorable to the different interface characteristics including smaller transition zone, shorter and fewer cracks, and smaller and fewer pores. In Fig. 4(e)–(f), the BSE images of the interface mixing zone present several representative cracks that are located at the boundaries between dendrites having different orientations, which is similar to the case in Sample 3. In Fig. 4(g)–(h), the IPF and phase maps reveal that the grain size of the FCC phase (CuCr1Zr alloy) is much larger than that of the BCC phase (M300) at the interface. The CuCr1Zr alloy has a heterogenous grain distribution with a size of around 30 μm whereas the M300 has acicular lath structure with laths of 5−20 μm in length and 1−3 μm in width. In the phase map, the boundary between FCC and BCC phases are rather distinct. Based on the band contrast and misorientation in Fig. 4(g)–(i), the BCC phase region has stronger lattice distortion and strain localization than the FCC phase region, which might be due to the finer grain structure. Notedly, the cracks appear at the melt pool boundaries where strain localizes. In summary, the cracks were formed either at the packet boundaries between dendrites having high misorientation or at melt pool boundaries with high strain localization.

The overall microstructure of Sample 2 after aging heat treatment is rather similar to that before aging. As can be seen, pores (Fig. 5(a)–(b)), defects like small cracks (Fig. 5(b)–(f)), and melt pool microstructure (Fig. 5(g)–(h)) were remained after aging heat treatment. Based on the IQ and KAM map in Fig. 5(i), a reduced localization of strain at the interface after aging heat treatment compared to Fig. 4(i) was observed.

Although the grain structure in the HAZ remains the same

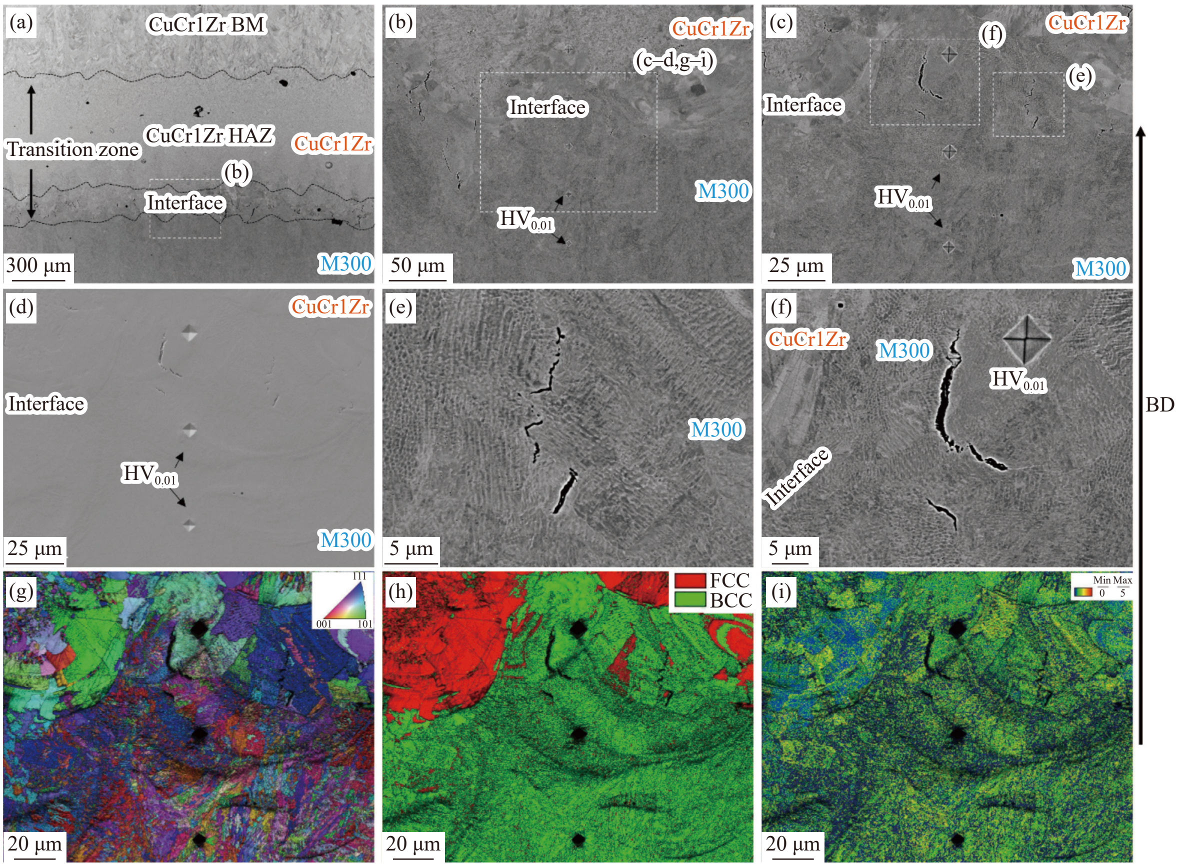

Fig. 4. (a–c, e–f) BSE images, (d) SE image, (g) IQ and IPF images, (h) IQ and phase map, and (i) IQ and KAM map across the interface between the M300 and CuCr1Zr of Sample 2 (CuCr1Zr on M300 with optimized parameters) before aging heat treatment.

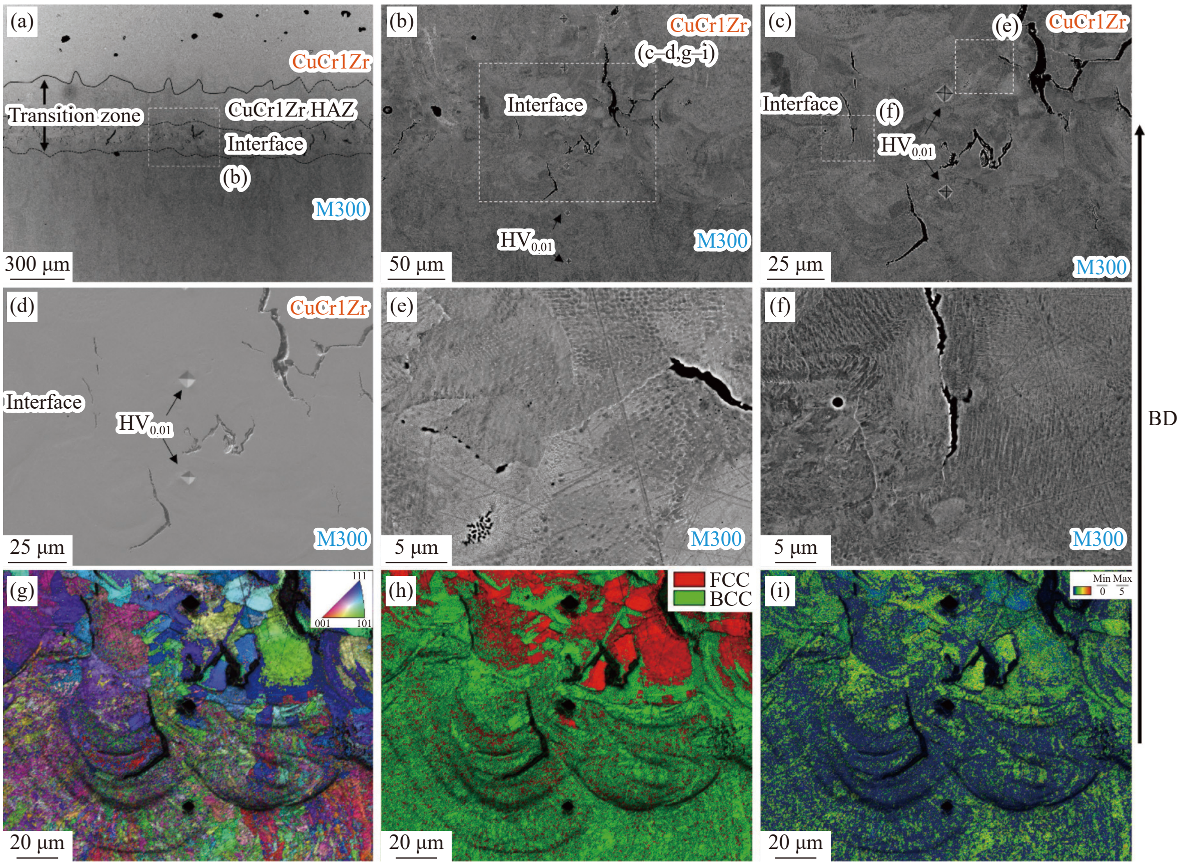

Fig. 5. (a–c, e–f) BSE images, (d) SE image, (g) IQ and IPF image, (h) IQ and phase map, and (i) IQ and KAM map across the interface between the maraging steel and CuCr1Zr of Sample 2 (CuCr1Zr on M300 with optimization) after aging heat treatment.

after aging heat treatment, the hardness profile across the interface in Samples 2 and 3 varies dramatically as displayed in Fig. 2. The variation is mainly correlated to the CuCr1Zr HAZ. In the as-built Samples 2 and 3, the CuCr1Zr in the HAZ was partially aged via IHT. The closer to the mixing zone the CuCr1Zr is, the more pronounced the IHT is, leading to higher hardness. The hardness gradient in the HAZ was eliminated by the post aging heat treatment, implying that the post heat treatment is capable of homogenizing the property of CuCr1Zr globally.

Although Sample 1 was manufactured by M300 deposited on CuCr1Zr, the microstructural images are displayed as CuCr1Zr alloy on the top in Fig. 6 for a direct comparison with Samples 2 and 3 in Fig. 3 and Fig. 4, respectively. The interface mixing zone is around 100 μm. Fig. 6(a)–(c) shows that a small amount of pores with a diameter up to 15 μm appeared in the M300 HAZ and mixing zone, and small cracks with a length up to 50 μm were parallel to the BD. Compared with Sample 2, Sample 1 showed slightly lower defect density (0.25% vs. 0.28%), as shown in Table 5.

Compared with Sample 2, Sample 1 has finer BCC grain structure (Fig. 6(g)–(h)) with acicular laths of up to 3 μm in length and 0.5−1 μm in width. Likewise, the melt pool is also slightly smaller. The occurrence of finer microstructure could be attributed to a combination of lower heat input and better conductivity of CuCr1Zr alloy.

As revealed in Fig. 4(h), Fig. 6(h), and Fig. 7(h), a more pronounced mixing of the FCC and BCC phases occured at the interface of Sample 1. Furthermore, the microstructure inside the melt pools at the interface was also finer as observed in the EBSD maps of Fig. 6(g)–(i) and Fig. 7(g)–(i).

The lattice distortion and strain localization in Sample 1 (Fig. 6(g) and (i)) seemed to be weaker than that in Sample 2. However, the locations of defects like small cracks in Sample 1 coincided well with those of the strain localization. The interface microstructure of Sample 1 after aging heat treatment was very similar to that before aging. The IQ and KAM map in Fig. 7(i) indicated a slightly reduced localization of strain at the interface after aging heat treatment.

The interface microstructure and defects of Samples 1−3 is summarized in Table 5. There is an evident improvement in interface integrity with the processing parameters optimization, e.g. reduced and smaller defects. Similar tendency was reported in the work of Tan *et al.* [38], which contributes to higher bonding strength between the BMs. Despite some defects present at the interface mixing zone, sound metallurgical bonding between M300 and CuCr1Zr were formed during the single-step multi-material PBF-LB process.

3.4. Thermal properties

Many factors can affect the thermal conductivity of bimetallic parts, such as solutes in the CuCr1Zr alloy, porosity in the matrix and locally at the interface, and lattice imperfection like boundaries. According to the previous work, aging

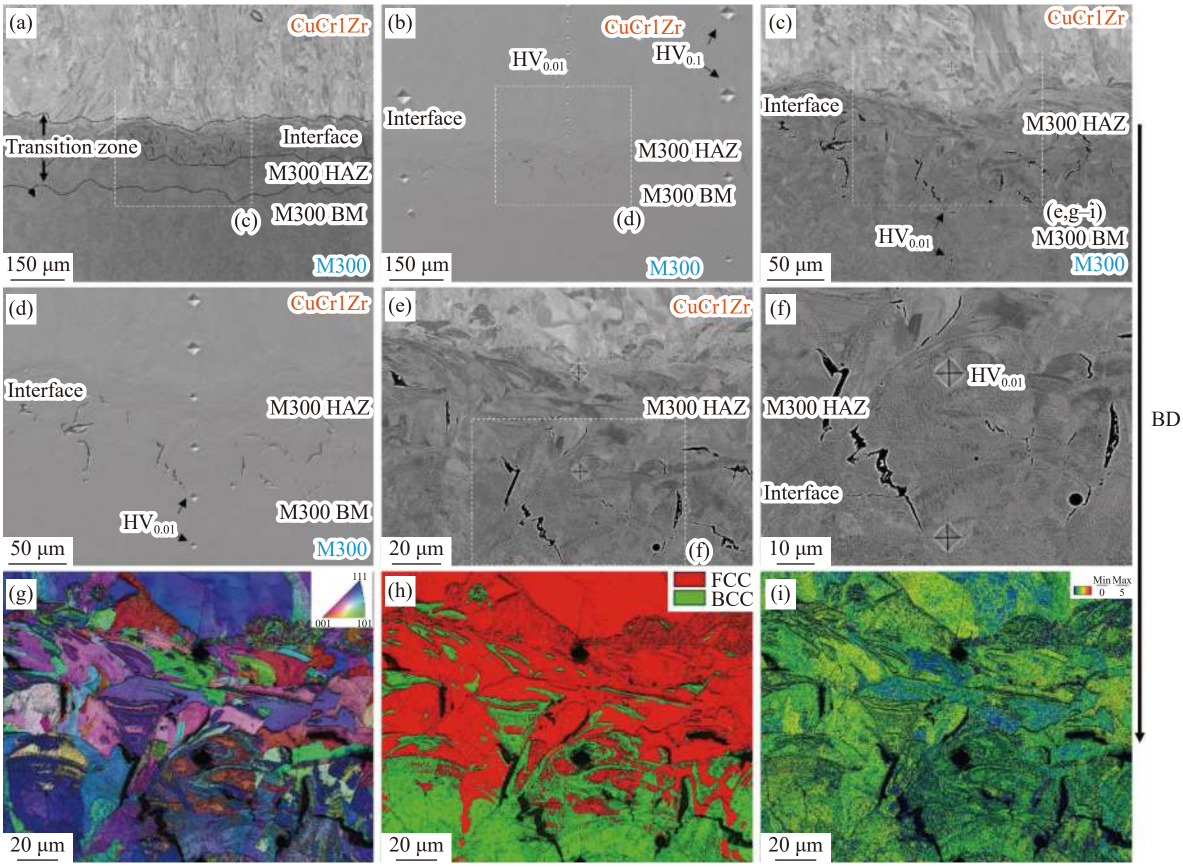

Fig. 6. (a, c, e–f) BSE images, (b, d) SE images, (g) IQ and IPF image, (h) IQ and phase map, and (i) IQ and KAM map across the interface between the maraging steel and CuCr1Zr of Sample 1 (M300 on CuCr1Zr with optimization) before aging heat treatment.

Table 5. Summary of the interface microstructure and defects in Samples 1−3

Samples	HAZ			Mixing zone		Defects in the interface mixing zone		
	Location	Size* / mm	Size** / mm	Size* / mm	Size** / mm	Density / %	Crack length / μm	Pore diameter / μm
1	M300	0.125	0.1	0.1	0.1	0.25	50	15
2	CuCr1Zr	1.150	0.1	0.1	0.1	0.28	50	70
3	CuCr1Zr	1.450	—	0.3	—	0.66	200	100

Notes: Size* represents the size of HAZ measured in the as-built samples; Size** represents the size of HAZ measured in the aging treated samples.

process triples the thermal diffusivity of the pure CuCr1Zr but has negligible influence on the thermal diffusivity of pure M300 steel, attributing to the consumption of solute atoms during the precipitation of the FCC phase. As a result, the thermal diffusivity of M300–CuCr1Zr after aging was measured to be twice of that of pure M300 steel [31].

A further increase of thermal diffusivity by approximately 40% is achieved in this work by tailoring parameters for the interface, seen in Sample 1 in Fig. 8, which could be attributed to the reduction of defect density at the interface resulted from the elimination of large lack-of-fusion defects. To certain extent, the thermal conduction can be facilitated by the reduction of misorientation and local strain across the interface as observed in the IQ and KAM maps especially in Fig. 4 and Fig. 5.

In comparison, the thermal diffusivity of Sample 2 remains similar to that of Sample 3 (Fig. 8), despite smaller and fewer defects at the interface (Table 5). This can be claimed to be caused by the porosity observed in the CuCr1Zr HAZ in Sample 3. Furthermore, Sample 1 shows much higher thermal diffusivity as compared with Samples 2 and 3. A large quantity of phase boundaries appear in the intermixing zone due to the immiscibility and the lattice mismatch between the FCC and the BCC phases. Regardless of the aging process, these high angle boundaries remain in the microstructure, having adverse effect on thermal conduction caused by the scattering of electrons and phonons. As summarized in Table 5, all aging treated samples have comparable mixing zone and HAZ, so the difference in thermal diffusivity is likely to be associated with the size and density of defects.

4. Conclusions and outlook

The multi-material M300–CuCr1Zr parts were manufactured via one-step PBF-LB process. The interface microstructure, hardness mismatch, and thermal properties of M300–CuCr1Zr parts with different configurations by PBF-

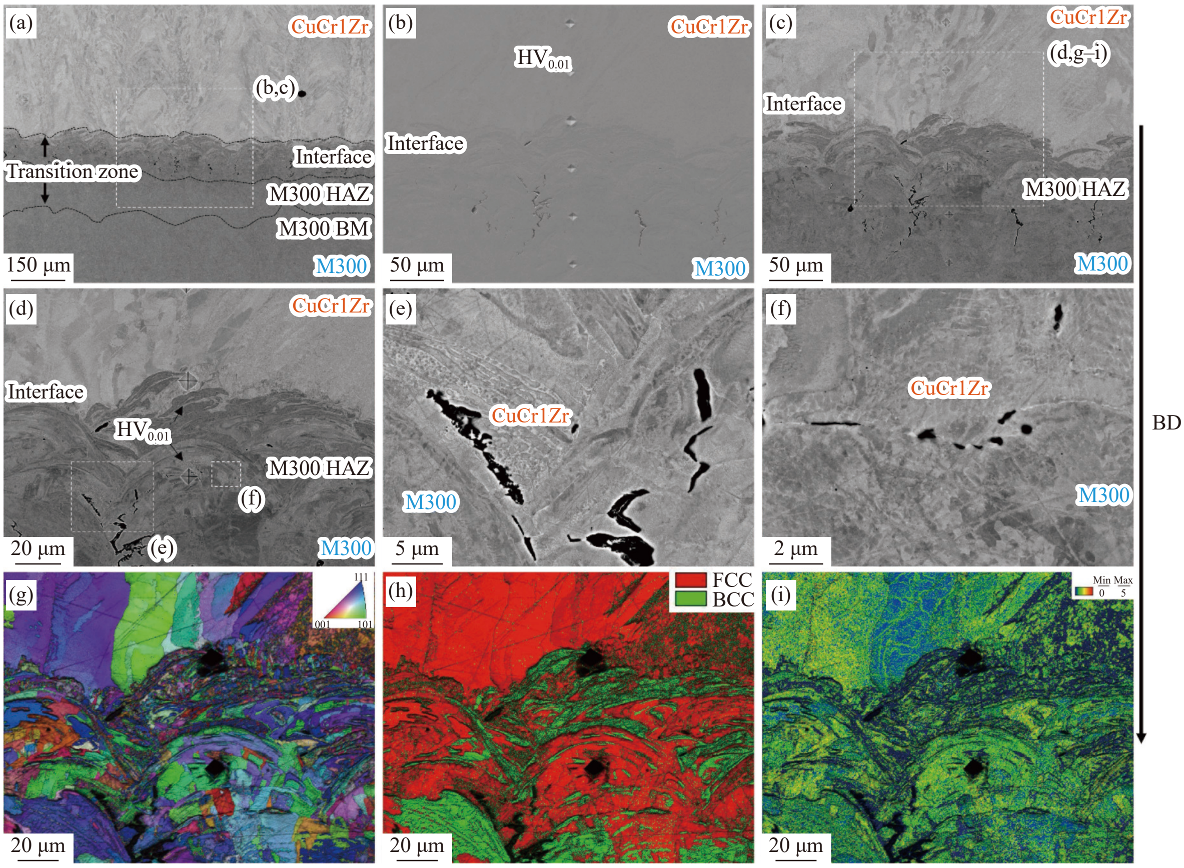

Fig. 7. (a, c–f) BSE images, (b) SE images, (g) IQ and IPF image, (h) IQ and phase map, and (i) IQ and KAM map across the interface between the maraging steel and CuCr1Zr of Sample 1 (M300 on CuCr1Zr with optimization) after aging heat treatment.

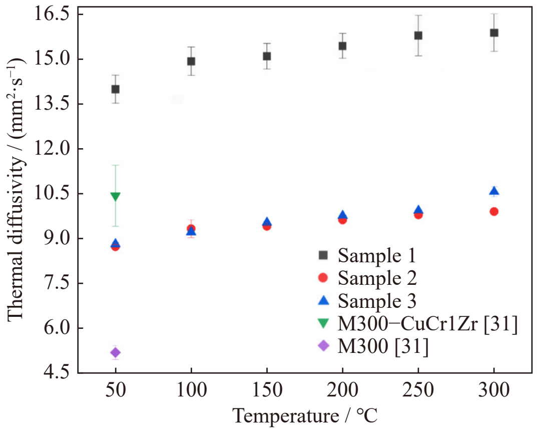

Fig. 8. Thermal diffusivity as a function of temperature of the aging treated Sample 1–3. As a comparison, the thermal data of pure M300 and M300–CuCr1Zr after aging are also plotted.

LB were investigated. The following conclusions can be drawn.

(1) The bi-metallic parts have dense cross section, implying that the present one-step multi-material PBF-LB is comparable to the conventional single-material PBF-LB.

(2) The interface microstructure, mixing zone width, and the defect quantities are dependent on the processing parameters. The defects at the interface reduced after introducing appropriate interface processing parameters, even in comparison with the normal welding processes of dissimilar metals.

(3) A one-step aging heat treatment can significantly enhance the mechanical properties of the M300 steel as well as the thermal properties of M300–CuCr1Zr parts. Furthermore, the aging heat treatment reduces the size of transition zone and the strain localization in the mixing zone.

(4) By using 50vol% of CuCr1Zr and optimized interface parameters for lowering defects at the interface, the thermal diffusivity of M300–CuCr1Zr increased by 150% compared to pure M300 steel.

Although the present work successfully demonstrates the capability of improving the thermal diffusivity of bimetallic M300–CuCr1Zr samples using tailored interface parameters, there are more future work to be carried out in order to mature the technology. Instead of uniform interface parameters applied in this study, a gradient of energy input could be developed with the assistance of simulation, which can further engineer the interface properties like mixing zone width, defect density and size. Additionally, hot isostatic pressing (HIP) can be considered to partially remove the defects located at the interface. The current aging parameters are not optimized for application and can be more extensively investigated to achieve higher thermal diffusivity while assuring demanded hardness.

Acknowledgements

The work is supported by VTT Technical Research Centre of Finland, Aalto University, Aerosint SA, and partially from European Union Horizon 2020 (No. 768775). The authors would like to express their gratitude for the experimental contributions from Nicolas Gianfolcaro of Aerosint, T. Lehtikuusi, J. Rantala, and J. Lukin of VTT. The utilization of the Academy of Finland's RawMatTERS Finland Infrastructure (RAMI) based at Aalto University, GTK Espoo, and VTT Espoo is acknowledged.

Conflict of Interest

The authors declare that they have no known competing financial interests or personal relationships that could have appeared to influence the work reported in this paper.

Open Access funding provided by Technical Research Centre of Finland.

References

[1] A. Kirchheim, Y. Katrodiya, L. Zumofen, F. Ehrig, and C. Wick, Dynamic conformal cooling improves injection molding Hybrid molds manufactured by laser powder bed fusion, *Int. J. Adv. Manuf. Technol.*, 114(2021), No. 1, p. 107.

[2] S.C. Feng, A.M. Kamat, and Y.T. Pei, Design and fabrication of conformal cooling channels in molds: Review and progress updates, *Int. J. Heat Mass Transf.*, 171(2021), art. No. 121082.

[3] J. Lee, J. Choe, J. Park, *et al.*, Microstructural effects on the tensile and fracture behavior of selective laser melted H13 tool steel under varying conditions, *Mater. Charact.*, 155(2019), art. No. 109817.

[4] K. Kempen, B. Vrancken, S. Buls, L. Thijs, J. Van Humbeeck, and J.P. Kruth, Selective laser melting of crack-free high density M2 high speed steel parts by baseplate preheating, *J. Manuf. Sci. Eng.*, 136(2014), No. 6, art. No. 061026.

[5] K. Bae, D. Kim, W. Lee, and Y. Park, Wear behavior of conventionally and directly aged maraging 18Ni–300 steel produced by laser powder bed fusion, *Materials*, 14(2021), No. 10, art. No. 2588.

[6] L. Wu, S. Das, W. Gridin, *et al.*, Hot work tool steel processed by laser powder bed fusion: A review on most relevant influencing factors, *Adv. Eng. Mater.*, 23(2021), No. 7, art. No. 2100049.

[7] A.G. Demir and B. Previtali, Multi-material selective laser melting of Fe/Al–12Si components, *Manuf. Lett.*, 11(2017), p. 8.

[8] M. Schneck, M. Horn, M. Schmitt, C. Seidel, G. Schlick, and G. Reinhart, Review on additive hybrid- and multi-material-manufacturing of metals by powder bed fusion: State of technology and development potential, *Prog. Addit. Manuf.*, 6(2021), No. 4, p. 881.

[9] C. Wei and L. Li, Recent progress and scientific challenges in multi-material additive manufacturing via laser-based powder bed fusion, *Virtual Phys. Prototyp.*, 16(2021), No. 3, p. 347.

[10] T. Bareth, M. Binder, P. Kindermann, V. Stapff, A. Rieser, and C. Seidel, Implementation of a multi-material mechanism in a laser-based powder bed fusion (PBF-LB) machine, *Procedia CIRP*, 107(2022), p. 558.

[11] M. Mehrpouya, D. Tuma, T. Vaneker, M. Afrasiabi, M. Bambach, and I. Gibson, Multimaterial powder bed fusion techniques, *Rapid Prototyping J.*, 28(2022), No. 11, p. 1.

[12] M. Schneck, M. Horn, M. Schindler, and C. Seidel, Capability of multi-material laser-based powder bed fusion—Development and analysis of a prototype large bore engine component, *Metals*, 12(2021), No. 1, art. No. 44.

[13] C. Singer, M. Schmitt, G. Schlick, and J. Schilp, Multi-material additive manufacturing of thermocouples by laser-based powder bed fusion, *Procedia CIRP*, 112(2022), p. 346.

[14] D. Wang, L.Q. Liu, G.W. Deng, *et al.*, Recent progress on additive manufacturing of multi-material structures with laser powder bed fusion, *Virtual Phys. Prototyp.*, 17(2022), No. 2, p. 329.

[15] C. Wei, L.C. Liu, Y.C. Gu, *et al.*, Multi-material additive-manufacturing of tungsten–copper alloy bimetallic structure with a stainless-steel interlayer and associated bonding mechanisms, *Addit. Manuf.*, 50(2022), art. No. 102574.

[16] Y.C. Bai, J.Y. Zhang, C.L. Zhao, C.J. Li, and H. Wang, Dual interfacial characterization and property in multi-material selective laser melting of 316L stainless steel and C52400 copper alloy, *Mater. Charact.*, 167(2020), art. No. 110489.

[17] J. Chen, Y.Q. Yang, C.H. Song, D. Wang, S.B. Wu, and M.K. Zhang, Influence mechanism of process parameters on the interfacial characterization of selective laser melting 316L/$CuSn_{10}$, *Mater. Sci. Eng. A*, 792(2020), art. No. 139316.

[18] J. Chen, Y.Q. Yang, D. Wang, Z.X. Liu, and C.H. Song, Effect of manufacturing steps on the interfacial defects of laser powder bed fusion 316L/$CuSn_{10}$, *Mater. Lett.*, 292(2021), art. No. 129377.

[19] J. Schanz, N. Islam, D. Kolb, *et al.*, Individual process development of single and multi-material laser melting in novel modular laser powder bed fusion system, *Prog. Addit. Manuf.*, 7(2022), No. 3, p. 481.

[20] Z.H. Liu, D.Q. Zhang, S.L. Sing, C.K. Chua, and L.E. Loh, Interfacial characterization of SLM parts in multi-material processing: Metallurgical diffusion between 316L stainless steel and C18400 copper alloy, *Mater. Charact.*, 94(2014), p. 116.

[21] S.L. Mao, D.Z. Zhang, Z.H. Ren, G. Fu, and X.Y. Ma, Effects of process parameters on interfacial characterization and mechanical properties of 316L/CuCrZr functionally graded material by selective laser melting, *J. Alloys Compd.*, 899(2022), art. No. 163256.

[22] C. Anstaett, C. Seidel, and G. Reinhart, Fabrication of 3D multi-material parts using laser-based powder bed fusion, [in] *2017 International Solid Freeform Fabrication Symposium*, Austin, 2017, p. 9.

[23] A. Cunha, A. Marques, F.S. Silva, *et al.*, 420 stainless steel–Cu parts fabricated using 3D multi-material laser powder bed fusion: A new solution for plastic injection moulds, *Mater. Today Commun.*, 32(2022), art. No. 103852.

[24] V. Lindström, O. Liashenko, K. Zweiacker, *et al.*, Laser powder bed fusion of metal coated copper powders, *Materials*, 13(2020), No. 16, art. No. 3493.

[25] S.D. Jadhav, L.R. Goossens, Y. Kinds, B. Van Hooreweder, and K. Vanmeensel, Laser-based Powder bed fusion additive manufacturing of pure copper, *Addit. Manuf.*, 42(2021), art. No. 101990.

[26] P.F. Guan, X.H. Chen, P. Liu, *et al.*, Effect of selective laser melting process parameters and aging heat treatment on properties of CuCrZr alloy, *Mater. Res. Express*, 6(2019), No. 11, art.

No. 1165c1.

[27] Z.B. Ma, K.F. Zhang, Z.H. Ren, D.Z. Zhang, G.B. Tao, and H.S. Xu, Selective laser melting of Cu–Cr–Zr copper alloy: Parameter optimization, microstructure and mechanical properties, *J. Alloys Compd.*, 828(2020), art. No. 154350.

[28] H.F. Xie, X.P. Tang, X.H. Chen, *et al*., The effect of build orientations on mechanical and thermal properties on CuCrZr alloys fabricated by laser powder bed fusion, *J. Mater. Res. Technol.*, 23(2023), p. 3322.

[29] R.P. Polkam, *Laser Powder Bed Fusion of CuNi2SiCr Alloy: Process Parameters Optimization and Electro-mechanical Characterization* [Dissertation], Politecnico di Torino, Torino, 2022.

[30] B. Neirinck, X.S. Li, and M. Hick, Powder deposition systems used in powder bed-based multimetal additive manufacturing, *Acc. Mater. Res.*, 2(2021), No. 6, p. 387.

[31] X. Li, N. Gianfolcaro, O. Dedry, and A. Mertens, Microstructure and properties of multi-material parts by PBF-LB, [in] *World PM2022 Proceedings*, Lyon, 2022.

[32] E.A. Jägle, Z.D. Sheng, P. Kürnsteiner, S. Ocylok, A. Weisheit, and D. Raabe, Comparison of maraging steel micro- and nanostructure produced conventionally and by laser additive manufacturing, *Materials*, 10(2016), No. 1, art. No. 8.

[33] C. Elangeswaran, K. Gurung, R. Koch, A. Cutolo, and B. Van Hooreweder, Post-treatment selection for tailored fatigue performance of 18Ni300 maraging steel manufactured by laser powder bed fusion, *Fatigue Fract. Eng. Mater. Struct.*, 43(2020), No. 10, p. 2359.

[34] B. Podgornik, M. Šinko, and M. Godec, Dependence of the wear resistance of additive-manufactured maraging steel on the build direction and heat treatment, *Addit. Manuf.*, 46(2021), art. No. 102123.

[35] C. Wallis and B. Buchmayr, Effect of heat treatments on microstructure and properties of CuCrZr produced by laser-powder bed fusion, *Mater. Sci. Eng. A*, 744(2019), p. 215.

[36] C. Salvan, L. Briottet, T. Baffie, L. Guetaz, and C. Flament, CuCrZr alloy produced by laser powder bed fusion: Microstructure, nanoscale strengthening mechanisms, electrical and mechanical properties, *Mater. Sci. Eng. A*, 826(2021), art. No. 141915.

[37] P. Kürnsteiner, M.B. Wilms, A. Weisheit, P. Barriobero-Vila, E.A. Jägle, and D. Raabe, Massive nanoprecipitation in an Fe–19Ni–xAl maraging steel triggered by the intrinsic heat treatment during laser metal deposition, *Acta Mater.*, 129(2017), p. 52.

[38] C.L. Tan, K.S. Zhou, W.Y. Ma, and L. Min, Interfacial characteristic and mechanical performance of maraging steel–copper functional bimetal produced by selective laser melting based hybrid manufacture, *Mater. Des.*, 155(2018), p. 77.